

Here is a sample  
chapter from  
*Practical Implemen-  
tation of Light Ion  
Beam Treatments*©.

**This sample chapter is copy-  
righted and made available  
for personal use only.** No  
part of this chapter may be  
reproduced or distributed in  
any form or by any means  
without the prior written  
permission of Medical  
Physics Publishing.

**You can order this book in one of two formats:**

**Hardcover:** ISBN 978-1-930524-55-2

**eBook:** ISBN 978-1-944838-64-4

**To order by phone, call MPP at 1-800-442-5778.**

## Chapter 1

# INTRODUCTION

### 1.1 Clinical Use of Light Ion Beams

Proton treatments of humans first began in 1954 in Berkeley, California (Lawrence 1957). Early work centered upon treating the pituitary gland for hormone suppression (Lawrence and Tobias 1956; Tobias et al. 1958). In 1957 Berkeley switched from protons to helium ions (Lawrence et al. 1962; Castro et al. 1980). In 1975 large field treatments began with helium ions and in 1977 with carbon and neon ions, in 1979 with argon ions, and in 1982 with silicon ions (Levy 2008). In this book, a **light ion** is defined, according to Chu et al. (1993), and later agreed upon by the International Commission on Radiation Units and Measurements (ICRU) (Wambersie et al. 2004), as having an atomic number less than or equal to 10 (neon). Treatment of ocular melanomas with helium ions began in 1978 (Castro et al. 1997) followed in 1980 by treatments of arteriovenous malformations (AVMs) (Fabrikant et al. 1992). Early treatment beamlines used scattering foils to generate a uniform lateral dose profile over the treatment area, but in 1986 use of a magnetic scanning system was begun (Renner and Chu 1987). The ion

treatment program finished in 1993 due to shutdown of the Bevalac accelerator that had been supported by the U.S. Department of Energy (Alonso and Castro 2002). Table 1.1 gives an estimate of the number of patients treated at Berkeley with different particles and accelerators. Exact numbers are difficult to provide because some patients were treated with more than one particle.

A proton treatment program was started in Uppsala, Sweden in 1957 (Falkmer et al. 1962). This human treatment program was notable for being the first to treat patients with proton beams for Parkinson's disease and chronic pain (Larsson et al. 1963). The program was also the first to scan the beam magnetically to provide a uniform lateral dose profile (Larsson et al. 1959).

In 1961 a proton program began in Boston, Massachusetts, for the treatment of pituitary disorders (Kjellberg et al. 1962). In 1965 the Boston group began treating AVMs (Kjellberg 1986). In 1974 large field treatments began for an assortment of diseases. A specialized program for the treatment of ocular melanomas was developed and began treating patients in 1975 (Gragoudas et al. 1985).

During the late 1960s, 1970s, and 1980s, several other proton programs began in Dubna, Moscow, and St. Petersburg, Russia (Dzhelepov and Gol'din 1969;

Table 1.1. Estimated number of patients treated at Berkeley

ion species	184-in. SC 1954–1987	Bevalac 1977–1993	total 1954–1993
$^1\text{H}^{1+}$	30	0	30
$^4\text{He}^{2+}$	2054	88	2142
$^{12}\text{C}^{6+}$	0	24	24
$^{20}\text{Ne}^{10+}$	0	299	299
$^{28}\text{Si}^{14+}$	0	20	20
$^{40}\text{Ar}^{20+}$	0	2	2
<b>total</b>	2084	433	2517

Goldin et al. 1989); Chiba and Tsukubu, Japan; Villigen, Switzerland; and Clatterbridge, England. In addition to treating the regular assortment of large tumors, ocular melanomas, and AVMs, the Russian programs are also noteworthy for having treated epilepsy (Konnov 1987), trigeminal neuralgia, and the uterus and upper third of the vagina using a transvaginal approach (Minakova and Burdenko 1987). The Chiba facility is noted for being the first to scan a small spot across the field to generate a **fluence**-modulated dose distribution (Kanai et al. 1980; Kawachi et al. 1983). By 1990 a total of 8,500 patients had been treated worldwide with protons and other light ions (Sisterson 1990).

Between 1974 and 1980, facilities at Los Alamos, New Mexico; Vancouver, British Columbia; and Villigen, Switzerland, began treating patients with negative pi-meson (pion) beams. Although not light ions, these charged particle programs were instrumental in developing the techniques and control systems currently being implemented for **energy- and fluence-modulated (EFM)** scanning with light ion beams. The large scattering by the lightweight pions and the high cost of operation resulted in the closing of all of these programs by 1994. At the end of the programs, Los Alamos had treated 228 patients (von Essen et al. 1987), Vancouver 367 (Sisterson 1995), and Villigen 503 (Sisterson 1995).

In 1990 Loma Linda University Medical Center (LLUMC) in Loma Linda, California, opened the first proton treatment facility with an accelerator and beamlines specifically designed for human treatments with protons and located inside a hospital. LLUMC was also the first facility to utilize isocentric rotating gantry-mounted beamlines. In 1994 LLUMC began treating macular degeneration and tumors in the lung. In 1998 this facility reached the milestone of using a proton beam to treat 100 patients per day and in 2005 treated 173 patients in one day.

Between 1990 and 2005, several other institutions around the world opened proton treatment facilities. During this same time period, LLUMC treated about 11,000 patients with proton beams, which was about one-third of all patients treated throughout the world with light ions. In 2009 approximately 475 patients per day were being treated with proton beams at six operating centers in the United States. Considering that there are approximately 1.4 million new cases of cancer in the United States every year and that approximately 60% of cancer patients receive radiation as part of their treatment, less than 0.6% of all radiotherapy patients were receiving proton beam treatments.

In 1994 Chiba, Japan, started treatments with carbon ions and had treated 4,504 patients through 2009. Darmstadt, Germany, started treatments with carbon ions in 1997 and had treated 384 patients as of 2007. Hyogo, Japan, opened a proton and carbon ion facility in 2002 and had treated 454 patients with carbon beams as of 2008. A research facility in Lanzhou, China, began treating patients with a low-energy carbon beam in 2006 (Li, Dai et al. 2007). New facilities capable of delivering carbon ion beams are currently being planned or built in Italy (2), Germany (3), Japan (1), Austria (1), and France (1). An updated list of all of the operating proton and other light ion facilities around the world including the number of patients treated at each may be found at the Particle Therapy Co-Operative Group website (<http://ptcog.web.psi.ch/ptcentres.html>).

There are two reasons for using ions heavier than protons. The first reason is related to the rate of energy deposition per unit depth that the ion traverses, the **linear energy transfer (LET)**. The LET is higher with carbon and oxygen ions than with protons, resulting in a greater **relative biological effectiveness (RBE)**. For carbon ions, the RBE increases with increasing depth, therefore yielding a higher effective dose relative to the surface than with proton beams. At the present time, carbon ions are indicated for advanced tumors of the prostate and cervix, localized lung tumors, esophagus, salivary gland, and tumors that have been shown to have increased sensitivity to high LET compared to their surrounding normal tissues. The second reason for using ions heavier than protons is that the larger mass of the heavier ions results in a reduced degree of scatter. Less scattering yields sharper beam edges, enabling higher dose gradients between diseased tissue and normal tissue. Helium ions are indicated for high geometric accuracy treatments such as ocular melanomas, macular degeneration, and AVMs. Carbon ions may be even more attractive than helium ions for small radiosurgical targets near critical structures such as found in Parkinson's disease. For the next few years, until further clinical research is performed, protons will likely remain the general-purpose beam. The physical characterization of ions heavier than protons is almost identical to that used with protons; only the biological optimization is significantly different. Most of the tests described in this book are, therefore, based upon established techniques with proton beams. Discussions of biological effect and optimization of light ions may be found elsewhere including the International Atomic Energy Agency (IAEA) report entitled "Dose Reporting in Ion Beam Therapy" (IAEA 2007).

Much of the development work in light ion treatments from 1998 to 2005 centered on the area of delivering EFM portals. The state of the art has progressed sufficiently that any new facility starting treatments later than the year 2007 should have EFM capability.

## 1.2 Treatment Process

The design and delivery of light ion treatments requires a chain of procedures similar to other novel radiation treatment approaches using high-energy photon and electron beams, such as intensity-modulated radiation therapy (IMRT), image-guided radiation therapy (IGRT), stereotactic radiosurgery (SRS), etc. Although the characteristics of light ion beams offer an ability to better limit delivery of dose only to those regions desired, those same characteristics can magnify the effects of any errors that occur in the process. Constant vigilance is therefore required in all steps of the process. The old adage “the devil is in the details” must never be forgotten in the application of light ion beams. Initial training and periodic retraining are essential aspects of light ion beam programs.

## 1.3 Functional Characteristics of Light Ion Beams

The rationale for light ion treatments is predicated on three basic elements. First, the low entrance dose and almost zero dose distal to the target results in the dose delivered to non-target tissues relative to the dose delivered to target tissues being much lower than for other radiation beams. Second, the lateral and distal dose gradients are higher, enabling better dissection of the target and normal tissues. The third, which only applies to ions heavier than helium, is that a differential RBE with depth results in a higher effective dose in target tissues compared to surrounding normal tissues.

### 1.3.1 Depth Dose

Figure 1.1 shows depth dose distributions for six non-range-modulated charged particle beams. Four of these distributions were measured with an ionization chamber in a water phantom (a, b, e, and f) while two of them (c and d) were simulated with the Monte Carlo program

MCNPX (Pelowitz 2005). Figure 1.1a is for a 6 MeV electron beam and should be familiar to most people working in radiotherapy. The dose rises slowly with depth to a maximum and then gradually drops. Figure 1.1b is for a 250 MeV proton beam. The dose is relatively constant with depth for most of its penetration, rises rapidly just before the particles lose all their energy, and then drops sharply almost to zero. Figure 1.1c is for a 200 MeV antiproton beam. This distribution is very similar to a proton beam except the peak is slightly broader and it has a long **tail**. Figure 1.1d is for a 218 MeV per nucleon helium ion beam. Its distribution also looks similar to that from a proton beam except the peak is a little narrower and the distribution has a small tail. Figure 1.1e is for a 290 MeV per nucleon carbon ion beam. The peak is even narrower than the helium beam and the distribution has a larger tail. Figure 1.1f is for a 969 MeV per nucleon iron ion beam. Although this charged particle beam would not be used for treatment, it is useful to show in a comparison because some of the features that are present only at small levels in the other beams are more apparent in this beam. The iron ion beam dose distribution has a large tail and both the entrance and tail regions decrease with depth.

Table 1.2 lists the various processes that occur with each beam to give them their characteristic shapes. With each beam, the stopping power increases as the energy of the particle decreases. This increase is small for electron beams but is the most important process for the other beams. A process that is very important for electron beams but is not important for any of the other beams is the increasing obliquity of the particles with depth leading to a buildup in fluence and thus dose. Straggling due to stochastic energy losses is a small effect for all of the beams. Straggling from multiple scattering paths is very important for electron beams, somewhat important for proton and antiproton beams, and less important for the heavier particles. Straggling due to the particles taking multiple paths through heterogeneities is surprisingly more important clinically for the heavier particles. This non-intuitive statement is because the smaller angle of scatter prevents the dose distribution from being blurred, resulting in localized regions of under- and overdose. Bremsstrahlung is only important for electron beams, as the heavier particles are moving too slowly for this effect to occur. Scatter from the **radiation head** (often referred to as a “nozzle” in light ion beam jargon) of the treatment unit is most important for electron beams because of their light weight; however, it cannot be ignored for the other beams. Nuclear attenuation is not important for electron

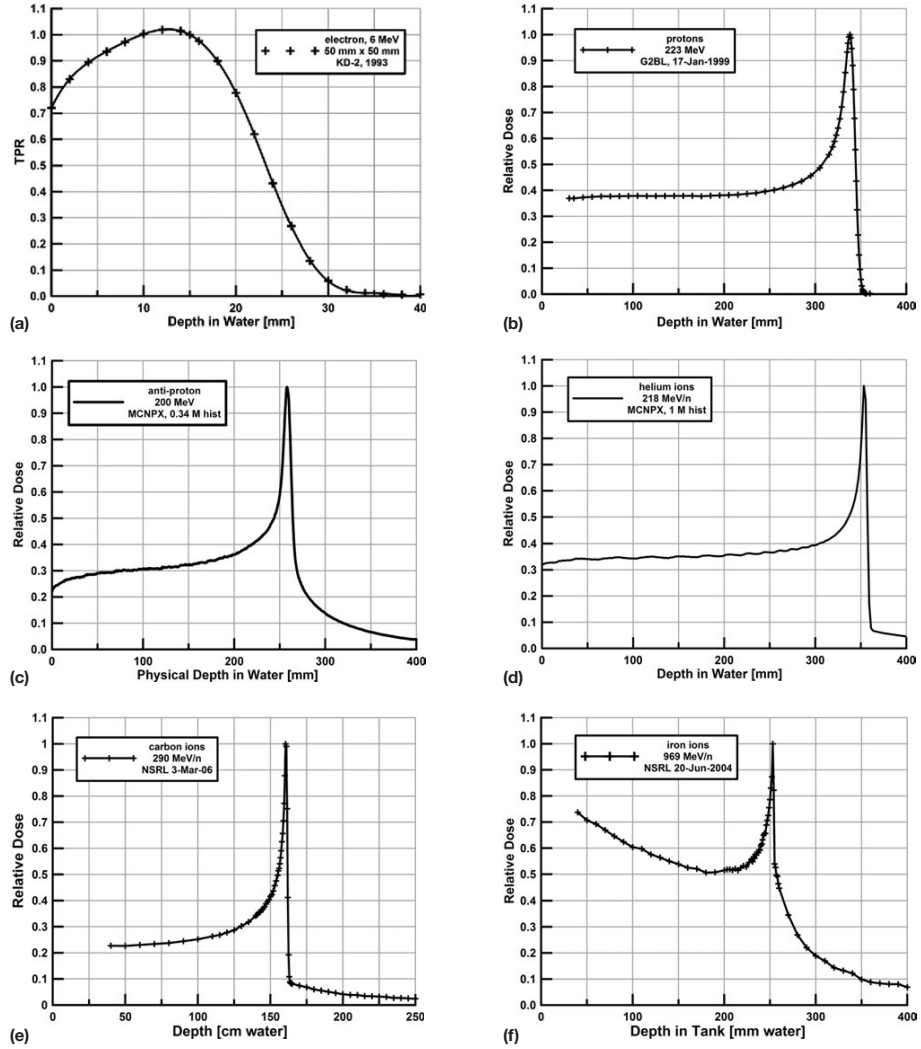


Figure 1.1. Depth dose curves for various charged particle beams. (a) 6 MeV electrons; (b) 223 MeV protons; (c) 200 MeV antiprotons; (d) 218 MeV/n helium-4; (e) 290 MeV/n carbon-12; (f) 969 MeV/n iron-56. All distributions are normalized to the dose at the peak. See text for descriptions of the features of each graph.

Table 1.2. Importance of various processes for different charged particles

particle	e	H-1	anti-H	He-4	C-12	Fe-56
increasing stopping power with decreasing energy	+	+++	+++	+++	+++	+++
increasing obliquity fluence buildup	+++	o	o	o	o	o
straggling from stochastic energy losses	+	+	+	+	+	+
straggling from multiple scattering paths	+++	++	++	+	+	+
straggling from multiple heterogeneity paths	+	++	++	+++	+++	+++
bremstrahlung	+	o	o	o	o	o
radiation head scatter	++	+	+	+	+	+
nuclear attenuation	o	+	+	+	+	++
buildup from secondary particles	++	+	+	+	++	+++
tail from secondary particles	o	+	+++	+	++	+++

beams, is slightly important for most of the light ions, and is very important for the iron ions because it leads to the descending shape of both the entrance and tail regions of its dose distribution. Buildup from secondary particles occurs in all beams. For electron beams, it is most obvious with a clean, well-collimated or scanned beam. It is difficult to see the effect on the depth dose distribution for proton beams, but it is, in fact, there. It is much more important for carbon and iron ions as both target fragmentation and projectile fragmentation occur in addition to delta ray production. Lastly, the tail from secondary particles is unimportant for electron and proton beams, is bothersome for helium and carbon beams, and very important for antiproton and iron ions. With antiprotons, this tail is not from fragmentation but rather from annihilation products and is directed not only in the depth direction but also to the sides. This

blurring of the dose distribution may reduce the beneficial effects of the high-RBE products, as it did during the pion beam trials during the late 1970s and early 1980s. Examples of dose distributions for patients treated with pion beams may be found in Hogstrom et al. (1979) and Pedroni (1981).

Figure 1.2 plots the electronic mass stopping power of various charged particles as a function of the remaining range of the particle. Notice that the stopping power increases with decreasing range for all particles, though not as much for the lightweight electron. Physicists and physicians working in radiotherapy should remember that electrons lose energy at a rate of 2 MeV per centimeter. The stopping power for the highest energy proton beam used clinically, 250 MeV (range equals 38 cm of water), is double that of the electron, i.e., 4 MeV per centimeter.

The minimum stopping power for a clinically used proton beam in water is twice that for an electron beam.

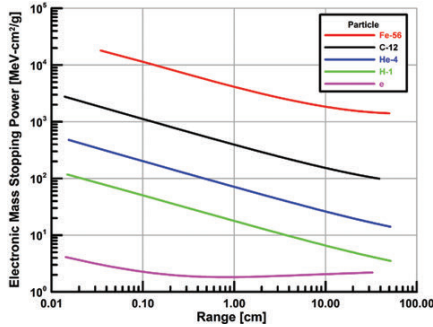


Figure 1.2. Electronic mass stopping power versus range in water for various charged particles.

The reason for an increase in stopping power with decreasing range is the speed of the particle. As a particle loses energy, its speed decreases and it has more time to interact with the molecules it is passing, thereby transferring more energy (Lapp and Andrews 1972). A derivation of the Bohr model of stopping power is given in the lecture notes by Fermi (1950) and descriptions and differentiation of different stopping power theories is given by Ziegler (1999). The reason that the stopping power of electrons does not change much with remaining range is that most of the energy of a fast electron is not in its speed but rather in its relativistic mass. For protons and heavier ions most of the ion energy is due to the speed of the ion. Table 1.3 gives the speed of various charged particles as a function of range.

Figure 1.3 shows the relative average energy deposition along the track of a single proton that started with an initial energy of 155 MeV. The dose distribution was calculated simply by dividing the depth into many thin slabs and calculating the dose deposited in each slab by multiplying the linear stopping power for the energy of the proton entering the slab by the thickness of the slab. If one were to look at a table of proton stopping powers, the maximum stopping power of a proton at the depth of the peak would be 185 times that of a proton entering the surface. On this plot, however, the peak-to-entrance dose ratio is only 29:1 because the energy deposition tallies were done in slabs a tenth-millimeter thick in the depth direction. This slab thickness is larger than the range of a proton with the highest stopping power, and thus the average energy deposition in the slab is lower than the maximum energy deposition possible for a proton. A measured depth dose curve yields an even smaller peak-to-entrance dose ratio of only about 4:1. Clearly, processes other than the change in stopping power contribute to the shape of the depth dose curve. For comparison, figure 1.4 is provided for an electron beam. One will notice that, along the track of a single electron, a peak does exist. The maximum stopping power at the peak of an electron is 27 times that at the surface; but for the size of the voxel used for scoring, the peak-to-entrance energy deposition on the plot is only about 2.5:1. As seen in figure 1.1a, the measured electron distribution usually only has a peak-to-entrance ratio of about 1.2:1. Again, the change in stopping power cannot be the only process shaping the depth dose curve.

One process that leads to a reduction in the peak-to-entrance dose ratio is straggling from stochastic energy losses. As seen in figure 1.5, protons (as do

Table 1.3. Speed relative to light of various charged particles

range [cm]	electron			proton			carbon-12		
	energy [MeV]	relative speed [v/c]	stopping power [MeV/cm]	energy [MeV]	relative speed [v/c]	stopping power [MeV/cm]	energy [MeV]	relative speed [v/c]	stopping power [MeV/cm]
0.1	0.34	0.80	2.09	8.83	0.14	49.7	196	0.18	1119
0.3	0.74	0.91	1.92	16.3	0.18	30.5	364	0.25	677
1.0	2.04	0.98	1.82	31.8	0.25	17.8	711	0.34	395
3.0	5.90	1.00	1.90	58.6	0.34	10.9	1314	0.44	247
10.0	21.8	1.00	2.05	115.1	0.45	6.56	2621	0.58	154
30.0	88.8	1.00	2.19	216.6	0.58	4.24	5092	0.73	107

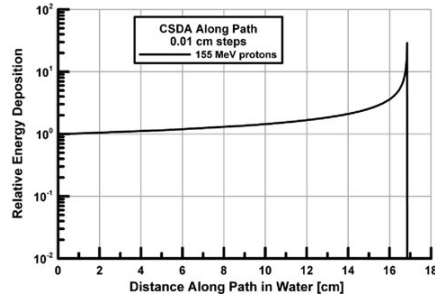


Figure 1.3. Continuous slowing down approximation (CSDA) depth dose for proton. Note that the energy deposition axis is logarithmic.

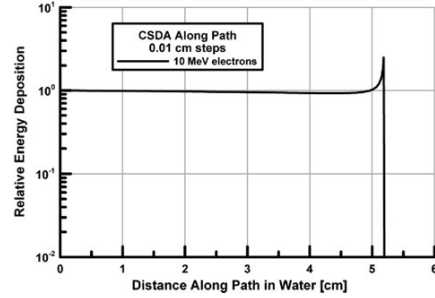


Figure 1.4. Continuous slowing down approximation (CSDA) depth dose for electron. Note that the energy deposition axis is logarithmic.

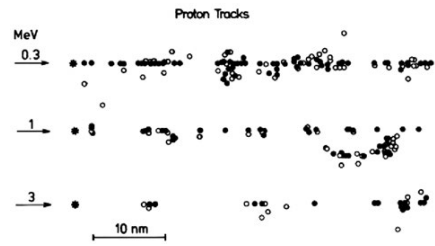
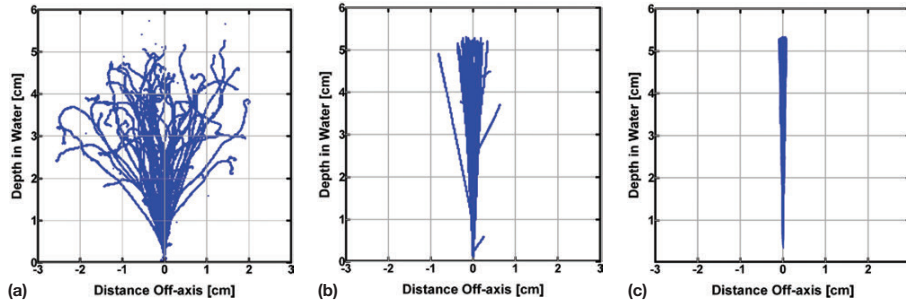


Figure 1.5. Discrete nature of energy loss leads to energy straggling. (Reprinted from Paretzke, H. G. "Advances in Energy Deposition Theory" in *Advances in Radiation Protection and Dosimetry in Medicine*, R. H. Thomas and V. Perez-Mendez (eds.), © 1980 with kind permission of Springer Science and Business Media.)

other ions) lose kinetic energy primarily in small discrete amounts as they undergo a multitude of interactions such as atomic ionization and elastic nuclear collisions. Not all protons will have the same number of interactions nor will each interaction have identical energy-transfer characteristics. An initially monoenergetic beam of protons will thus acquire a small energy spread after passing through an absorber. This energy straggling process is important if one is calculating a dose distribution from basic principles or writing a Monte Carlo simulation program but generally does not enter into a clinical physicist's daily life at a light ion treatment facility. Discussions about straggling due to

energy loss can be found in Janni (1982) and International Commission on Radiation Units and Measurements Report 73 (ICRU 2005).

Another process, one that is considered frequently in a physicist's daily practice, is straggling due to the particles of the beam taking multiple paths as they pass through the patient. Figure 1.6 shows plots of particle paths as they penetrate water. These paths were calculated with the Monte Carlo program MCNPX (Pelowitz 2005). Figure 1.6a shows the paths for 50 electrons each starting with an energy of 10 MeV. One sees that the electrons stop at a myriad of different depths. Even though the dose distribution along the path of each electron has a peak as seen in figure 1.4, these peaks are located at different depths. For a given depth, the total dose from all electrons is due to some large energy depositions and some small energy depositions. Figure 1.6b is for 50 protons each starting with an energy of 80 MeV. Although some of the protons stop at different locations, most of them tend to stop within 1 cm of each other so that most of the large energy depositions are close to one another and most of the small energy depositions are close to one another. This coherent stopping produces an easily measurable peak of energy deposition with respect to depth. Figure 1.6c shows 500 carbon ions each starting with an energy of 150 MeV per nucleon. Almost all carbon ions follow the same path and stop at the same location. This makes a very coherent energy deposition pattern resulting in a peak-to-entrance dose ratio for the carbon ion beam that is much closer to the single particle distribution than is seen with either the proton or electron beams.



**Figure 1.6.** Lateral scattering for point monodirectional beams of (a) 10 MeV electrons, (b) 80 MeV protons, (c) 150 MeV/n carbon ions. Straggling in depth occurs because of the multiple paths of the different particles.

Yet another form of straggling occurs when a laterally broad beam passes through a medium consisting of different materials. Figure 1.7 shows how ions traversing equal water equivalent depths can scatter and stop along a measurement line at different depths. As the degree of heterogeneity increases, the distal slope of the depth dose distribution measured along the line becomes shallower. This phenomenon must be kept in mind during treatment planning. Urie et al. (1986a) have studied this effect using protons, carbon ions, and neon ions as seen in figure 1.8.

Before deconstructing a proton depth dose distribution, it is useful to review the components of an electron depth dose distribution. Figure 1.9 shows a depth dose distribution for an electron beam with different regions color coded (Refer to color figures on attached DVD). Near the surface, electrons ionize atoms generating secondary electrons. A buildup of these secondary electrons occurs in the first few millimeters of depth until an equilibrium condition is met. This is shown in the far left [medium gray (magenta)] region. Build-up curves for several different energy electron beams are given by Sibata and de Almeida (1980). In the dark gray (blue) region the paths of the primary electrons become more tortuous with many electrons traveling obliquely with respect to their original direction. This results in an increasing fluence and hence dose as depth increases. Brahme and Svensson (1976) state that in “clean” beams this section is often concave upwards. The light gray (green) region represents where electrons have traveled far enough along their paths that they run out of energy and stop. Because each electron has taken a different tortuous path (see figure 1.6), the small peaks

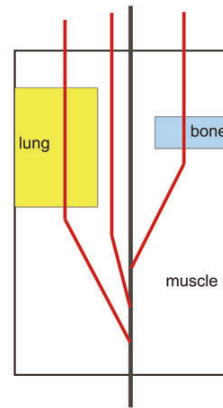


**Figure 1.7.** Illustration demonstrating straggling due to protons taking paths through different materials. Ions enter the muscle phantom from the top of the figure. Dark gray (red) lines represent paths of three separate ions. The thick black vertical line represents a line along which dose measurements are made. The ion that passed through the medium gray (light blue) bone material on the right and scattered to the measurement line stopped at a shallower depth than the ion that passed through the muscle. The ion that passed through the light gray (yellow) lung material on the left and scattered to the measurement line stopped deeper than the ion that passed through the muscle. A depth dose distribution measured along the black line near the end of range would thus have a shallower dose gradient with depth than if the phantom had been made entirely of muscle.

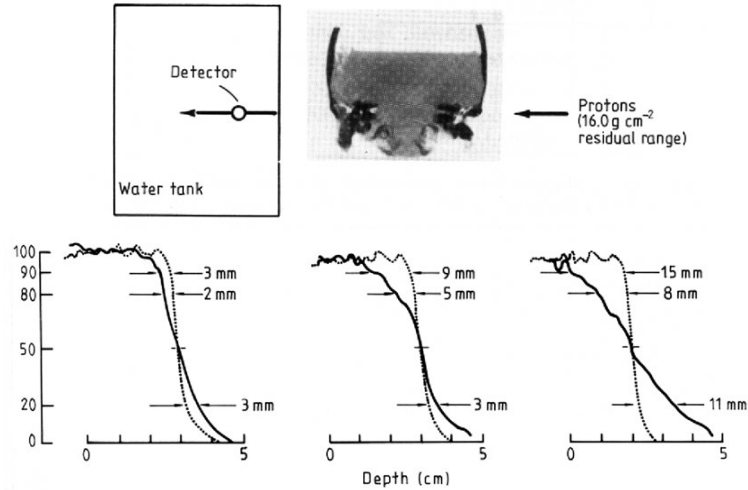


**Figure 1.8.** Experimental setup and results showing effect of straggling due to protons taking paths through different materials. The dotted curve in each graph represents a standard depth dose distribution measured in water. The solid curves represent depth dose distributions measured along different lines in the head phantom (superior and inferior to arrow) with varying degrees of heterogeneity. (Reprinted from *Physics in Medicine and Biology*, vol 31, issue 1, "Degradation of the Bragg peak due to inhomogeneities," M. Urie, M. Goitein, W. R. Holley, and G. T. Y. Chen, pp. 1–15, © 1986a with permission from the author and IOP Publishing, Bristol, UK.)

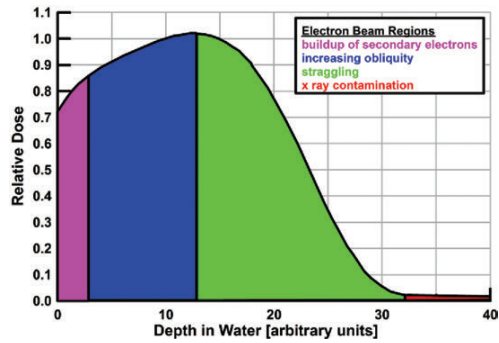


**Figure 1.9.** Regions of electron beam depth dose distribution.

near the end of their paths are located at many different depths resulting in an overall gradual decrease in dose. Finally, the far right region (medium gray/red) represents dose from contaminating bremsstrahlung produced in the head of the treatment unit and in the shallower layers of the patient.

Figure 1.10 shows that the proton depth dose distribution, shown in light gray (green), is slightly simpler than an electron depth dose distribution. Secondary electrons and delta rays are produced at all depths, but the range of these electrons is quite small. Secondary protons are also produced and a small build-up region is present near the surface, but it is often difficult to see. It is most easily observable with broad, high-energy beams where low-energy protons scattered off of the collimators do not mask the buildup. Beyond the build-up region there are two competing processes. The most apparent process is the increasing stopping power. The other process is a decrease in the number of protons due to nuclear interactions. These nuclear interactions remove the primary protons from the beam but can add neutrons, secondary protons, helium ions, carbon ions, and other particles. The solid black (blue) curve shows the number of primary protons remaining at each depth. Once the protons slow down and reach their peak energy

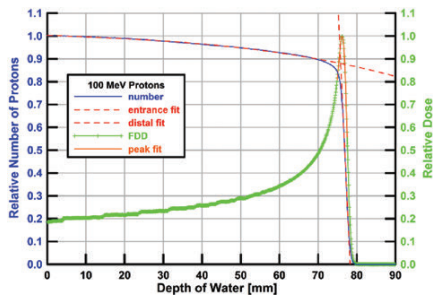


**Figure 1.10.** Proton beam depth dose and depth number distributions calculated with MCNPX. The solid black (blue) thin curve indicates the number of primary protons per unit depth normalized to the entrance value. The two dashed (red) curves are fits to the proton number curve; one in the region where primary protons are lost due to nuclear interactions (nearly horizontal) and one where primary protons lose their remaining energy and stop (nearly vertical). (Adapted from Moyers et al. (2007a) with permission from American Association of Physicists in Medicine.)

deposition rate, the protons run out of energy and stop. As shown earlier, however, not all protons stop at the same depth and so the fractional depth dose (FDD) distribution just beyond the peak is not represented by a vertical line but instead a line with a steep slope.

Figure 1.11 shows a magnified view of figure 1.10 centered on the peak region. The range of a proton beam is defined as being the depth where half of the protons stop. This does not mean half of the protons that were incident upon the surface but half of the protons that continued to cause ionization to the terminal depth. In this case of a 100 MeV beam, only about 88% of the protons survived, and the range is defined where 44% of the protons are remaining.

Figure 1.12 shows, by the dashed (red) curve, the fraction of protons remaining at the range as a function of range. The function is slightly curved because the nuclear interaction cross section is not constant for all energies. A linear fit to the data would give a 0.8% per centimeter probability of nonelastic nuclear interactions, but most people generalize to 1%. For low proton energies, this proton loss mechanism is relatively unimportant, but for high energies, more than 30% of the protons are lost before they lose all of their energy through ionization and stop.

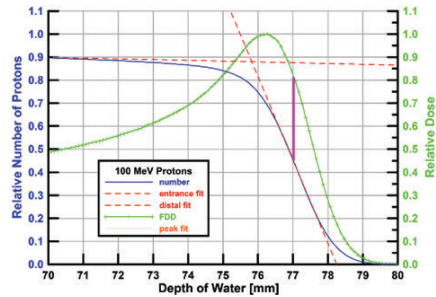


**Figure 1.11.** Same data as in figure 1.10 but expanded to emphasize the distal region. The vertical dark gray (magenta) line illustrates that the range (50% proton number) corresponds to the depth where the dose is 80.7% of the peak dose. (Adapted from Moyers et al. (2007a) with permission from American Association of Physicists in Medicine.)

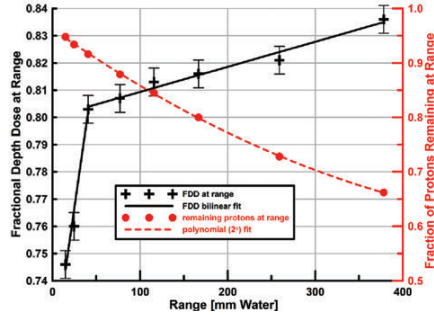


Figure 1.12. Depth dose and fraction of protons lost versus range. (Reprinted from Moyers et al. (2007a) with permission from American Association of Physics in Medicine.)

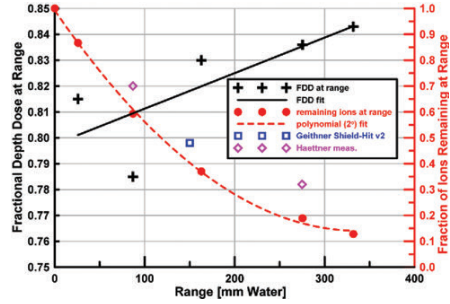


Figure 1.13. Depth dose and fraction of carbon ions lost versus range.

Proton beams lose about 1% of protons through nuclear interactions for every centimeter of water they traverse.

The black curve on the graph gives the FDD at the depth of the proton beam range. Equations (1.1) and (1.2) describe the relationship between range and fractional depth dose of a non-modulated proton beam.

ranges  $\leq 41.5$  mm,

$$\text{FDD} = ((2.263 \times 10^{-3}) * \text{range}) + 0.710 \quad (1.1)$$

ranges  $> 41.5$  mm,

$$\text{FDD} = ((9.166 \times 10^{-5}) * \text{range}) + 0.800 \quad (1.2)$$

Data similar to figures 1.10 and 1.11 have been generated for carbon ion beams using a non-released version of MCNPX extended to all ions (Moyers et al. 2005b, 2006a; James et al. 2006). Figure 1.13 plots FDD at the range and the fraction of incident carbon ions remaining at the range. As with proton beams, the carbon ion range is found at approximately the same depth as the 80% depth dose. Although this version of the Monte Carlo program has not been verified through extensive benchmarking, the calculated number of remaining carbon ions compares favorably with measurements and calculations presented by Haettner (2006) and Geithner et al.

The depth of the 80% of maximum dose for a non-modulated beam of protons approximately matches the depth where 50% of the protons are lost due to energy loss through ionization.

Carbon ion beams lose about 4% of carbon ions through nuclear interactions for every centimeter of water they traverse.

(2006), respectively. The results are sufficiently in agreement that the above rule of thumb can be provided.

Thus far this chapter has only discussed ion beams that are nearly monoenergetic. The width of the peak of the depth dose distribution is, however, too narrow to adequately treat most targets within a patient. A dose distribution that delivers an adequate dose to a finite size target can be generated by applying several beams with slightly different energies and relative fluences in rapid succession. Typically the difference in energy between these beams is chosen to give a range difference in the patient that is no more than roughly one-third of the full width at half maximum (FWHM) of the peak of the non-modulated distribution (Hsi et al. 2009a). The beams to produce an energy-modulated portal can be extracted directly from the accelerator at the required energies or, alternatively, different thicknesses of material can be inserted into the beam path to shift the range in the patient to different depths. In the latter case, the material may be placed completely across the beam and changed sequentially, a so-called **range shifter**, arranged around a rapidly spinning axle like a **propellor**, formed into pyramids or cones, or consist of multiple ridges, a so-called **ridge filter** (Chu et al. 1993; Moyers 1999). Usually the material has a low

atomic number to reduce scatter and to maintain efficiency of transport of particles through the radiation head. Occasionally, such as when a propellor is placed at the entrance of the radiation head, the difference in scattering between the thick and thin portions of the propellor becomes important so a high atomic number **scatter compensator** is added to the low atomic number propellor (Gottschalk 1987). Figure 1.14 is a graph showing the individual components that combine to make a uniform dose distribution with depth to cover a desired target. The uniform high-dose region is referred to as a **mesa** (Fowler 1981). The relatively uniform region between the surface and the mesa is referred to as a **plateau**.

Typically, the depth of the 90% dose of an energy-modulated portal is 1 mm less than the depth of the 90% dose of the highest energy non-modulated beam that is used to form the portal. Hsi et al. (2009a) have discussed the implications of different energy spreads entering the upstream end of the radiation head on the dose uniformity across the mesa and on the distal edge dose gradient. If the energy is varied before entering the radiation head, such as by extracting ions directly from the accelerator at the desired energy, then the **distal penumbra** width decreases with decreasing range

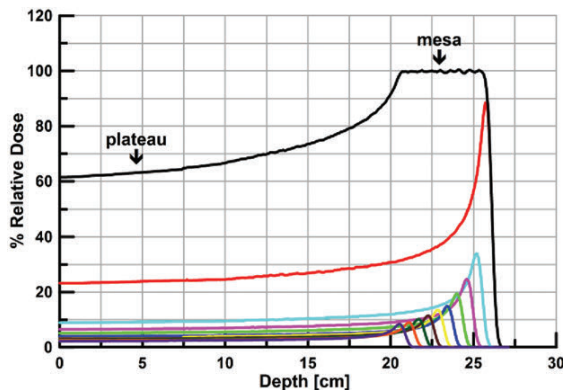


Figure 1.14. Depth dose distributions for multiple beams of different energies and fluences that are combined to give a uniform depth dose curve over a finite size target.

The distal penumbra,  $DP_{90-50}$ , of an energy-modulated proton portal is approximately 1.6% of the combined water equivalent thickness of the radiation head components and the water equivalent range in the patient.

in the patient. If the energy is varied within the radiation head, such as by inserting slabs of material, then the distal penumbra is constant with decreasing range in the patient. For the Loma Linda University Proton Treatment Facility (LLUPTF) synchrotron and a double scattering system (see discussion below) that produces a field size of 22 cm diameter, the 90% to 50% distal penumbra is approximately 0.016 of the water equivalent range in the patient ( $WER_{pat}$ ) added to the water equivalent thickness of the radiation head components ( $WET_{rh}$ ) through which the beam passes; that is,  $0.016 * (WER_{pat} + WET_{rh})$ .

When discussing energy-modulated portals in light ion treatments, there are four alternate definitions of range used in addition to the one shown in figure 1.11. Figure 1.15 shows three of these additional definitions. For purposes of dosimetry, such as looking up a stopping power value, the IAEA dosimetry Code of Practice, TRS-398, (IAEA 2000) defines the practical range as being the depth where the dose drops to 10% of the peak dose or **center of mesa (COM)** dose distal to the peak or mesa. This definition is required because using the “half remaining fluence” method shown in Figures

1.10 and 1.11 would result in negative ranges at some depths where ions are still penetrating. The American Association of Physicists in Medicine (AAPM) and the International Electrotechnical Commission (IEC) had, however, previously defined the term “practical range” for electron beams as the depth where a line tangent to the distal edge distribution intercepts a line extrapolated from the tail distribution. Because of this conflict of definitions, the 10% depth is referred to in this book as the **dosimetric range**, as seen in figure 1.15. The **residual range** is defined as the difference in depth between the dosimetric range and a point of interest. As an example, if the point of interest is at the nominal COM, a typical location to determine the dose per monitor unit, the residual range would be the depth of the dosimetric range minus the depth of the nominal COM.

As discussed in chapter 6, radiobiological principles suggest that the entire target should be covered by at least 90% of the dose prescribed to the target. This has led to a fourth definition of range, the **prescribed range**. This range, the depth at which the dose drops to 90% of the peak dose or COM dose is also presented in figure 1.15. The prescribed range is the definition that

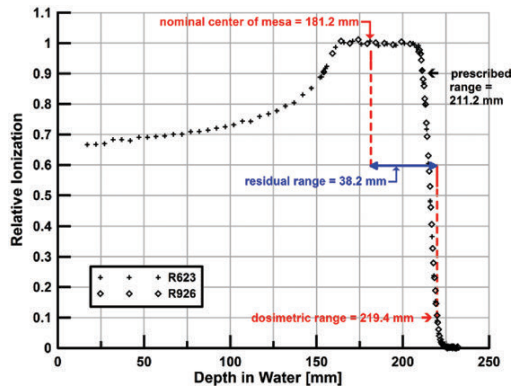


Figure 1.15. Illustration of the definitions for dosimetric range ( $R_{10}$ ), prescribed range ( $R_{90}$ ), nominal center of mesa, and residual range ( $R_{res}$ ). The two different symbols represent two data acquisition runs separated by several weeks, demonstrating reproducibility of ranges.

Table 1.4. Summary of range types

type	definition
beam	depth that corresponds to 50% of the non-attenuated primary ion fluence or depth that corresponds to $\approx 80\%$ of peak dose of non-modulated beam (see figures 1.10 and 1.11)
dosimetric (practical)	depth that corresponds to 10% of COM or peak dose (see figure 1.15)
residual	depth between interest point and depth that corresponds to 10% of COM or peak dose (see figure 1.15)
prescribed delivered	depth that corresponds to 90% of COM dose (see figure 1.15) prescribed range plus $WET_{rs}$ plus $WET_b$

most people working in ion therapy deal with on a daily basis. The prescribed range, however, is typically different for different off-axis positions because of irregular target shapes and the desire to protect normal tissues just distal to the targets. One method to accomplish this is to differentially modify the penetration depth of the ions at different off-axis positions by inserting a three-dimensionally shaped **bolus** of material into the beam path. The **delivered range** of the beam produced by the accelerator and radiation head and incident upon the bolus must therefore be larger than the prescribed range by an amount equal to the water equivalent thickness of the bolus,  $WET_b$ , at each off-axis position. In addition, if the beam delivery system is limited to a few steps of energy, then a uniform thickness sheet of material, called a **range shifter**, can be inserted into the beam path to reduce the ion energy. In this case, the water equivalent thickness of the range shifter,  $WET_{rs}$ , must also be added to the prescribed range to obtain the delivered range. Table 1.4 provides a summary of the various range definitions.

### 1.3.2 Lateral Profiles

The beam that is delivered to the radiation head is typically a few millimeters in diameter. This beam must be spread laterally across the patient to cover the target, which may be from 2 mm to 800 mm wide. The most common **lateral spreading devices (LSDs)** are scatterers and magnets, but with some delivery systems the patient is moved. It is also common to combine different types of LSDs.

Scatterers come in many different styles and are used in a variety of techniques. The design of scattering systems is beyond the scope of this book, but the various techniques are worth mentioning so the potential

purchaser of a **beam delivery system (BDS)** can converse with the manufacturer and understand the shape of the produced profiles.

The simplest scattering technique is to insert into the beam path a single thin foil of high atomic number. This technique creates a Gaussian-shaped lateral dose profile at the patient's location. To provide a dose uniformity of  $\pm 2.5\%$ , the efficiency of ion use is only 5% (Koehler et al. 1977). This low efficiency reduces the potential dose rate delivered to the patient, requires extensive shielding outside of the primary beam, and generates a large number of neutrons per dose of ions delivered to the patient. On the other hand, because all of the light ions emanate from a small spot on the foil, the effective source diameter is small, leading to a small lateral penumbra at the patient. This technique is generally only used for radiosurgery and targets within the eyes where a small lateral penumbra is important and field sizes are less than 40 mm diameter.

The most common scattering technique uses two scatterers with the second scatterer displaced downstream from the first scatterer by 20% to 30% of the distance from the first scatterer to the isocenter. The design process of shaping the lateral fluence profile using a combination of scatterers can be described mathematically as creating a square dose profile function using a sum of Gaussian profiles placed side by side. Although many different design techniques are available, none have produced an absolute square profile function necessitating the use of collimators to trim the peripheral non-uniform dose beam. In the past, occluding rings were placed adjacent to a uniform thickness second scattering foil to block some of the protons (Koehler et al. 1977). This technique has generally been abandoned because the efficiency of use was only 20% to 30% (Gottschalk 2009). Another

technique has been to place thin rings in the low-fluence (peripheral) part of the profile created by the first scatterer to scatter ions back into the useful beam (Takada 1994). The most common dual scatterer technique uses a contoured second scatterer. The early concepts for contoured second scatterers utilized a Gaussian-shaped radial thickness profile (e.g., Montelius and Brahme 1983) but later the shape evolved into a freeform profile determined using various optimization methods (e.g., Moyers and Siebers 1995). For proton beams this has resulted in a proton use efficiency of 40% to 50%. A consequence of the contoured design, however, is that the energy of the beam changes with off-axis distance because of the different thicknesses of scattering material. Fortunately, the uniformity in range across the beam can be restored by using a complementary **range compensator** made of a low atomic number material that reduces the range of the higher energy ions but produces very little scatter (Gotschalk et al. 1990). Figure 1.16 shows the thickness profile

used in a Monte Carlo simulation (Moyers 2003) of a beamline configured for 250 MeV protons to produce a 180-mm diameter field size with a 90% to 90% diameter of 164 mm. A feature of the contoured second scatterer design is that ions that hit near the center of the scatterer are scattered into wide Gaussian distributions, while those ions that hit near the periphery are scattered into narrow Gaussian distributions. Having narrow scattering distributions around the periphery helps steepen the dose profile near the desired lateral edge of the field. Figure 1.17 shows a profile of the produced dose distribution without any collimators installed. In the profile of figure 1.17 the dose increases slightly with increasing distance away from the axis before dropping sharply. This feature is a design trade-off between high ion use efficiency and uniformity. The distribution can be made flatter at larger radial distances at the expense of a lower dose rate and more neutron production outside the field. Figure 1.18 shows a lateral dose profile with a patient aperture installed.



**Figure 1.16.** Thickness profile of contoured second scatterer used in MCNPX simulation of beamline. The lead scattering material is shown in black and the PMMA range compensating material is shown in gray (yellow) (Moyers 2003a).

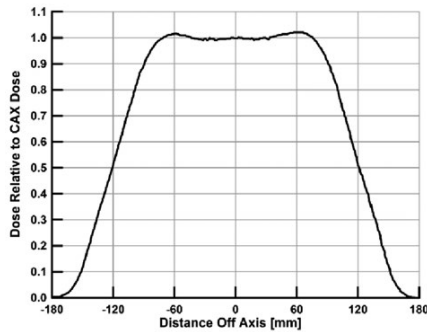


**Figure 1.17.** Lateral dose profile produced by contoured second scatterer measured at isocenter at depth without final pre-collimator plates or patient aperture.

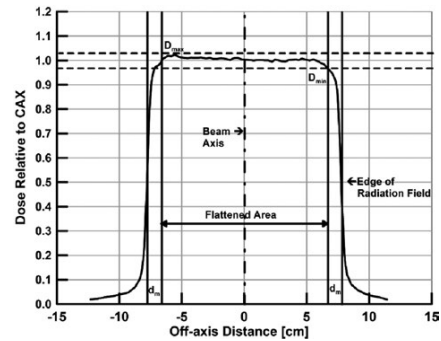


**Figure 1.18.** Lateral dose profile from contoured scatterer with Lipowitz metal aperture.  $d_m$  is the distance inwards from the edge of the radiation field that defines the region of the field over which the dose uniformity (flatness) is evaluated.

Unlike most electron beam treatment units that provide only a few discrete energies and scatter the electrons to a single field diameter for all possible beam applicators (cones), light ion beam treatment units usually allow a continuously variable energy selection and the beam is only spread laterally to the diameter necessary to provide a uniform fluence distribution across the beam applicator being used. This is done to maximize the dose rate, to minimize neutron production, and to minimize shielding requirements. For beams that use scattering systems, however, this demands many different combinations of thickness distributions of the high and low  $Z$  (atomic number) materials. Usually 4 to 10 second scatterers are mounted on one or more revolving carousels to support up to four different beam applicator sizes and the full range of ion energies. These are then used with a variable thickness first scatterer device which can come in a variety of different forms including but not limited to a carousel of foils, a binary combination of foils, or a double wedge configuration (Moyers et al. 1993; Moyers and Siebers 1995). Some systems also allow the first or second scatterer to be displaced towards and away from the isocenter to vary the dis-

tance between the scatterers (Hsi et al. 2009b). Some systems combine all or part of the first scatterer with an upstream modulator propellor (Gottschalk 1987).

An alternative to spreading the beam laterally with scattering foils is to scan the beam either mechanically or magnetically across the desired field. The simplest method of scanning uses a non-modulated beam flux to cover the field with a uniform fluence. This method is referred to as **uniform scanning**. A variety of scan paths can be used for this method, such as a Lissajous, multiple circles, spiral, or rectilinear. Figure 1.19 shows examples of these scan patterns. The Lissajous pattern (see figure 1.19a) is formed by scanning the beam in perpendicular directions with different frequencies that are not multiples of each other such that the path seldom repeats itself. It is the same pattern that was used successfully for many years with electron beams such as provided by the 40 MeV Sagittaire and 20 MeV Therac-20 linear accelerators. For these treatment units, the scanning frequencies were 0.615 Hz in the slow direction and 4 Hz in the fast direction (Ertan et al. 1984). The first patients treated with proton beams with a uniform scanning pattern were performed in Uppsala,

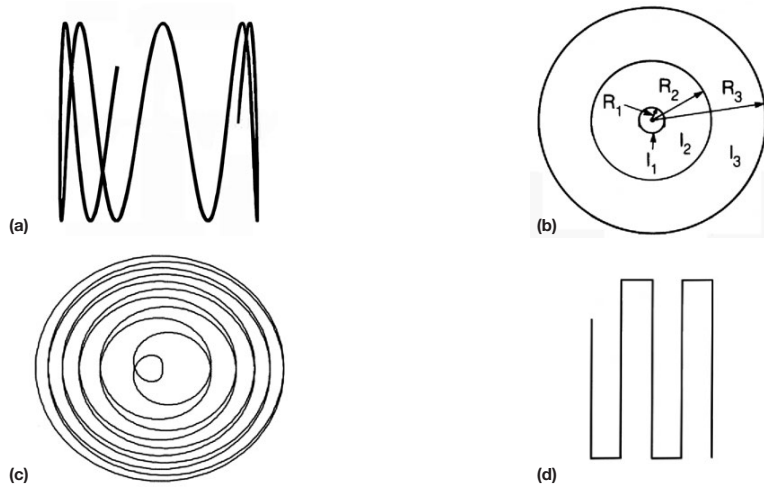


**Figure 1.19.** Uniform scanning patterns. (a) Lissajous; (b) multiple radii circles with different beam fluxes (adapted from Renner and Chu 1987); (c) small spiral (adapted from Anferov 2009); (d) rectilinear. (Adapted with permission from American Association of Physicists in Medicine.)

Sweden in 1957 (Larsson et al. 1959). During the 1980s, Berkeley scanned their ion beams heavier than helium with multiple circles of different radii (see figure 1.19b) to avoid fragmentation of the ions that would occur with scattering foils (Renner and Chu 1987). The circles were formed by rotating the beam using perpendicular magnets energized with sine waves 90° out of phase. The frequency of rotation for each radius was a fast 60 Hz to ensure that the dose distribution would be acceptably uniform with random starts and stops. One of the disadvantages of this system is that the constant rotation frequency required different beam fluxes for different radii, complicating the control system. Anferov (2009) has recently developed a spiral pattern for circular fields that does not require a change in beam current (see figure 1.19c). Both the Lissajous and multiple radii circular scanning patterns have sometimes been referred to as “wobbling.” In the case of the Lissajous scan pattern, this name seems appropriate because the beam follows a different path each pass across the field. Some Japanese proton and carbon ion facilities use a single radius circular scan pattern but in combination with a thin scattering foil to enlarge the spot size (Kanai et al. 1999), but the efficiency of beam use is only about 20% to 30% (Yonai et al. 2008). For small fields such as produced for an eye or radiosurgery cone, a small circular pattern with a relatively small FWHM spot diameter works well because: (1) there are a small number of scan positions that can be repeated very quickly; and (2) the collimators can be lightweight because little shielding is required to cover the small tails of the narrow Gaussian spots. The proton facility at Indiana University has tested a number of different patterns but as of 2008 used, for their large field treatments, only a rectilinear pattern (see figure 1.19d) that was repeated rapidly. Figure 1.20 is a lateral dose profile of a medium size, uniform scanned field using this style of scanning pattern. Uniform scanned fields may also be generated using closely packed triangle patterns or sine wave magnet currents that are repeated very rapidly (Chu et al. 1993). Use of the sine wave method is attractive because the scanning magnets and their power supplies can be configured in a resonance condition that permits repeated scanning at a high frequency while using little power. Such a system was developed by Martin (1992) with scan frequencies in perpendicular directions of 240 Hz by 4 Hz. This could be particularly advantageous for treating moving tissues. The number of neutrons produced by a uniform scanning system can be better or worse than a scattering system depending upon the overscan margin used. In particular, a rectangular scan pat-

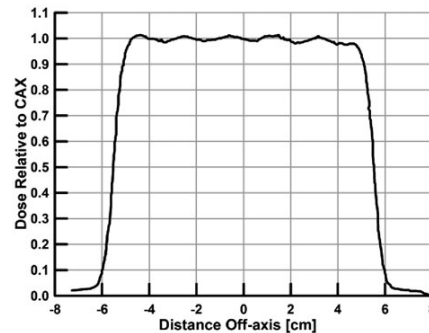


**Figure 1.20.** Lateral dose profile from uniform scanned field with brass aperture. Compared to fields produced with scatterers, uniform scanning fields usually have less asymmetry but some ripple due to imperfect matching of spot shape with scan path. Data for plot was taken from Farr et al. (2008).

tern should not be used with a circular applicator (cone). The amount of overscan can be minimized by using a pseudorectilinear pattern that matches the desired field shape (Young and McColl 1991). This proposed method uses a rectilinear scan pattern, but the extent of lateral scanning for each line is truncated just outside the projection of the aperture. This method maximizes the ion usage efficiency and minimizes the number of neutrons produced for irregularly shaped fields.

The last method of spreading a beam laterally is referred to as **modulated scanning** because different fluences can be delivered to different areas within the treatment field. The first modulated scanning with proton beams was performed in Japan by first collimating a beam to a small square and then magnetically aiming the square spot in two dimensions to many locations (Kanai et al. 1980). This method was referred to as “pixel scanning.” Later, the group at Villigen, Switzerland, developed a modulating scanning method by moving the patient positioner rapidly interspersed with individual Gaussian spots of beam delivery (Pedroni et al. 1995). This mechanical method of scanning is similar to what was used by Skaggs et al. (1958) and Rosenthal et al. (1969) for their 5 to 50 MeV electron beams except, in the proton case, one of the directions is scanned magnetically. This mechanical method is somewhat slow so most facilities prefer not to scan the patients but rather use magnets to scan the beam in both directions. As with uniform scanning, modulated scanning can use several

different methods for the selection of spot locations and scan paths. Most systems use one upstream magnet for one direction and a separate downstream magnet for the perpendicular direction. Because the opening in the upstream magnet is smaller and can thus scan faster, early investigations utilized constant path rectilinear patterns with the longer path between direction changes being scanned with the faster upstream magnet. This constant path scanning has sometimes been referred to as “raster scanning” due to the long parallel paths of scanning (the word raster derives from the Latin word *rastrum* meaning rake). The fluence in different areas of the field was modulated by varying either the beam flux, speed of the beam scanning, dwell time at discrete aiming locations, or a combination. After experience was obtained with real patient treatments, the fluence modulation requirements for each energy layer field was found to supersede the speed advantage of the upstream magnet. It is now more common that the scanning path does not follow a rectilinear raster pattern, although the aiming positions usually remain on a rectilinear grid. Several groups have developed path optimization algorithms; for example, Kang et al. (2007a), Pardo et al. (2009), and Trofimov and Bortfeld (2003). Path optimization is probably more important for delivery techniques that do not turn off the beam between aiming points as some dose is still delivered during the rapid move between points. Figure 1.21 shows how a scan path may be optimized to reduce both the overall path-length (and time) and the dose delivered in areas that should receive no dose.

In addition to dose uniformity, the other important parameter of lateral profiles is the **lateral penumbra (LP)**. The edge of a beam is usually defined as the off-axis position where the dose is 50% of the dose at the central axis of the beam. The lateral penumbra is usually defined, for purposes of acceptance testing, as the difference in off-axis distances between the 80% and 20% doses ( $LP_{80-20}$ ). This definition is used because the dose gradient in this region is typically linear with off-axis distance. On the other hand, the typical criterion for designing a field for a patient is to have the tumor covered by 90% of the dose prescribed near the center of the tumor. The parameter of choice for placing a margin around a target in a patient during treatment planning is thus the distance between the off-axis points where the dose is 90% and 50% of the central axis dose ( $LP_{90-50}$ ).

For most ion beams, the lateral penumbra width increases with depth primarily because of **multiple**

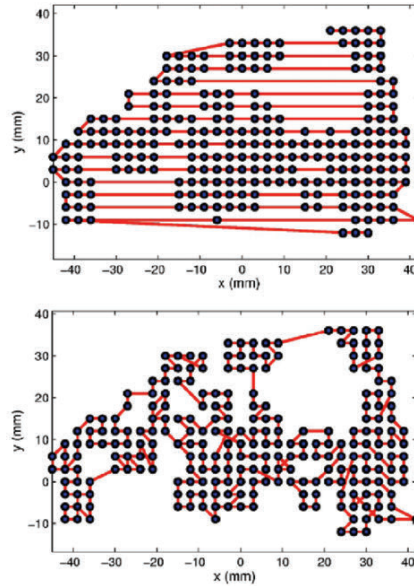


**Figure 1.21.** Aiming points for scanning beam. Top: Standard raster path; bottom: Optimized path. (Reprinted from Kang, J. H., J. J. Wilkens, and U. Oelfke, “Demonstration of scan path optimization in proton therapy.” *Med Phys* 34(9):3457–3464, © 2007a with permission from AAPM.)

**Coulombic scattering (MCS)** within the patient. For proton beams, the lateral penumbra increases significantly with depth and can get quite large. Carbon ions are much heavier than protons and thereby scatter much less (see figure 1.6). The explicit consideration of the penumbra width in treatment planning is thus more important for proton beams than with carbon ion beams. For uniform dose fields created with scatterers, the lateral penumbra is also a function of the effective source diameter, which is typically 20 to 30 mm. Some beamlines change the range in the patient by inserting range shifters into the middle of the radiation head. For this type of beamline, the effective source diameter increases with decreasing range because increasing range shifter thickness increases ion scattering within the radiation head and therefore the angular distribution of ions exiting the radiation head. For beams that use

The lateral penumbra,  $LP_{90-50}$ , of a proton portal is approximately 3% of the water equivalent depth (WED) in the patient for minimal gaps between the final aperture and patient surface.

apertures, a larger air gap between the aperture and patient results in a larger lateral penumbra because of the projection of the effective source diameter. Scatter from and transmission through the apertures can also contribute to the penumbra width, particularly near the surface. This is because the ions coming from the aperture have reduced energies and travel at larger angles with respect to the central axis compared to the primary ions. The aperture contribution can depend upon whether the aperture has diverging, parallel, or converging sides and the air gap between the aperture and the patient. For scanning beams without apertures, the scatter of ions within the radiation head from the vacuum window, beam monitors and air can be a major contributor to the penumbra width. Detailed consideration of the lateral penumbra as a function of several variables have been published by Urie et al. (1986b), Oozeer et al. (1997), and Safai et al. (2008). For the LLUPTF synchrotron, a double scattering system that produces a field size of 22 cm diameter, and a patient aperture placed close to the patient's skin (30 to 70 mm), the  $LP_{90-50}$  is approximately 0.03 of the water equivalent depth (WED) in the patient. Specifications for penumbra values as a function of penetration depth and ion species are given in chapter 3.

The margin to account for the lateral penumbra of beams formed using the delivery technique of modulated scanning without apertures and boluses is more difficult to define than with collimated beams as it varies at different locations around the field. This is because the aiming spots are usually discretized on a rectilinear array of spots thus preventing optimal conformance of the beam edge to the target and optimal conformal avoidance to adjacent normal tissues. This problem applies to both the lateral field edge and the distal field edge. Figure 1.22 illustrates the lateral field edge problem in a plane perpendicular to the beam axis. The intersections of the gray grid lines represent possible locations to which the beam may be aimed. The thick black curve represents the desired edge of the field. To achieve sufficient dose at the field edge, spots must be placed just outside the desired field edge. Depending upon the location of the grid points with

respect to the desired field edge, an insufficient margin of the first row of spots requires a second row of aiming points outside the field. At these locations, marked with bold crosses, the edge of the beam will be further from the target than desired. One method to reduce this problem is to use **contour scanning**. This method begins by scanning the beam at an optimal margin around the edge of the field and then fills the inside of the field with similar but smaller scan paths. Figure 1.23 shows a hypothetical scan pattern using contour scanning. A variation on this technique is to scan the periphery with very small diameter spots and the interior with larger diameter spots. As of 2009, no light ion facility was using contour scanning.

An issue similar to the problem of using a rectilinear aiming grid for scanned beams occurs when **multi-leaf collimators (MLCs)** are used with light ion beams. In addition to the discreteness of the dose distribution due to leaf widths, the penumbra also depends upon the design of the leaves and their material. Calculations performed by Svensson et al. (2007) showed that use of a leaf edge consisting of 30 mm thick tungsten or, even better, osmium, can minimize edge scatter and completely absorb most light ion beams for ranges up to about 260 mm of water, thus sharpening the tail of the lateral dose distribution. For low-energy beams, use of an MLC may be preferable to modulated scanning without apertures because of the unavoidable large beam spot sizes generated by scattering in the radiation head.

In addition to the penumbra width affecting the quality of dissection of the tumor and normal tissues, the increasing penumbra width with increasing depth has a significant impact on the depth dose for narrow fields. This effect is manifested in what appears to be a field size effect. Figure 1.24 shows the depth dose distribution for a proton beam for several different field sizes. It appears that the peak-to-entrance ratio is changing with field size. In reality, as the field size decreases, the penumbras from opposing sides of the field begin to overlap at the center of the field, decreasing the delivered dose. Because the penumbra becomes larger with depth, the dose at depth decreases faster with decreasing field size than near the surface, reducing the

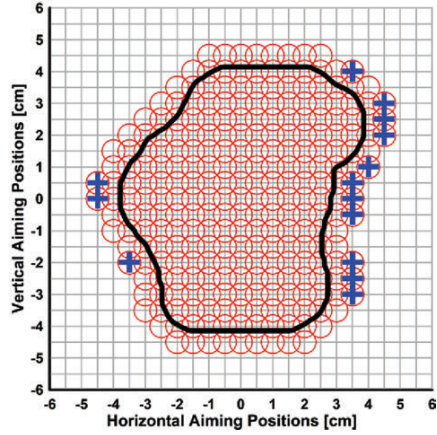


Figure 1.22. Scanned beam aiming points versus desired field. The solid black curve represents the desired field edge. Circles represent the spots aimed at the various locations. Crosses represent locations where the field margin will be larger than desired to maintain adequate dose at the field edge.

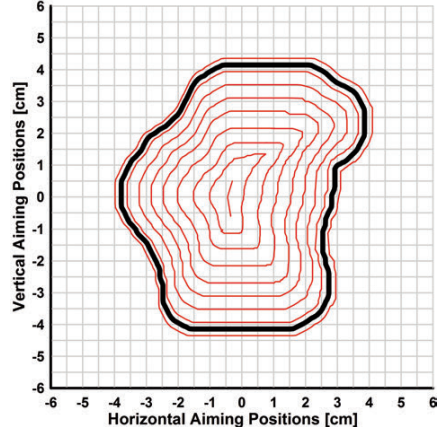


Figure 1.23. Technique of contour scanning. The solid black curve represents the desired field edge. The light gray (red) curves represent the path of the center of the scanning beam.

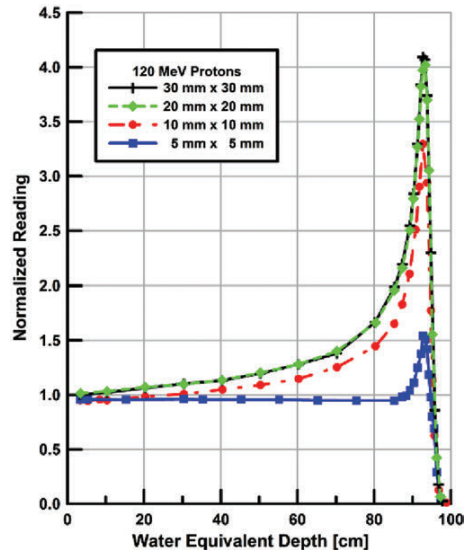


Figure 1.24. Depth dose distributions for several field sizes of a proton beam.

For proton fields having diameters less than the range of the beam divided by 8, changes in the depth dose distribution occur.

depth dose at depth. Figure 1.25 illustrates both effects for a deeply penetrating beam. Empirical data for different energies and field sizes has shown the above rule of thumb.

An additional field size effect occurs because of the contribution from neutrons (and some large angle scattered ions) produced laterally beyond the range of MCS scattered primary ions. Pedroni et al. (2005) have shown that this **halo** contribution is important for accurate predictions of the dose per monitor unit (MU). This contribution increases with increasing field size.

Another type of field size effect has to be taken into account when performing absolute dosimetry of spot scanning delivery with small proton beams in different phantom materials. It was demonstrated by Schneider et al. (2002b) that a difference in dose of 2.3% was found between measurements in water and polymethyl methacrylate (PMMA) phantoms at a WED of 150 mm for a 177 MeV small diameter proton beam. This difference

in dose is observed because the number of protons scattered away from the beam center by inelastic nuclear processes was different in the two materials. Dose measurement procedures for different phantom materials and small beam sizes are discussed in detail in chapters 2 and 8.

### 1.3.3 Scattering from the Aperture, Bolus, and Patient

Dosimetry for light ions shares similarities with dosimetry for high-energy photon and electron beams. What makes light ion dosimetry difficult is taking into account scattering from the aperture, bolus, and patient under conditions that are dissimilar from reference calibration conditions. This scattering can cause changes in the penumbra width, creates dose inhomogeneities within the patient, and dramatically changes the dose per monitor unit so that the

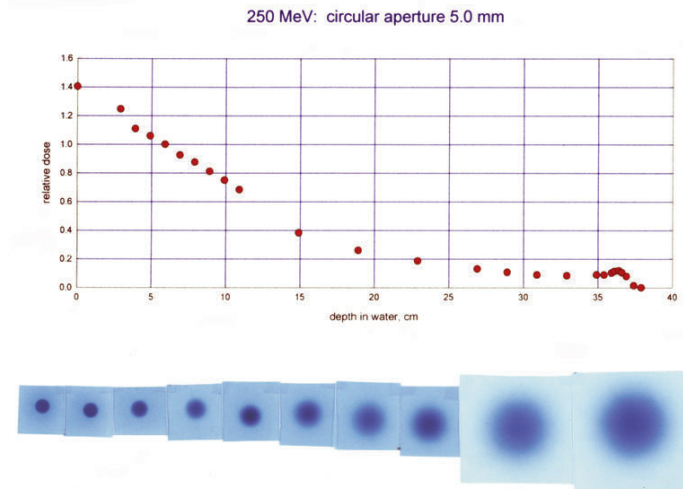


**Figure 1.25.** Depth dose distribution for a monoenergetic 250 MeV proton beam shaped with a 5-mm circular aperture. Depth dose distribution was obtained from radiochromic films (series of films are presented below the graph).

standard rules of thumb do not apply. Even the best calculation models may not be sufficiently accurate; therefore measurements of the dose may need to be performed for these non-reference conditions to obtain a better dose estimation. The equipment and procedures to perform these measurements are given in chapter 2, applications for commissioning for treatment are given in chapter 8, and applications for patient-specific quality assurance are given in chapter 10.

#### 1.4 Uncertainties, Deviations, Tolerances, and Errors

Throughout this book many measured and calculated results are given and discussed. There are several important aspects for which the user should remain aware. When analyzing the results of the measurements and quantifying the uncertainties, the user should clearly distinguish absolute accuracy from precision or reproducibility. The user should also understand the policies in establishing tolerances and setting up corrective actions. This section briefly outlines the definitions and relationship between uncertainties, deviations, tolerances, and errors that are established by the International Organization for Standardization (ISO 1994, 1995).

The uncertainty of the result of a particular measurement generally consists of several components which the International Committee of Weights and Measures (CIPM) groups into two categories according to the methods used to estimate their numerical values. Type A uncertainties are evaluated by statistical methods and can be estimated from repeated independent observations—these are usually expressed as a standard deviation (SD). Type B uncertainties can only be estimated by an analysis of the process under consideration and assigning reasonable variations to parameters where the uncertainties are not exactly quantifiable. Type A uncertainties are associated with precision whilst type B uncertainties contribute to absolute deviations from the correct value. Type A uncertainties of a random nature from different sources are generally added in quadrature. Overall uncertainty is a combination of both type A and type B uncertainties. Uncertainties of both types can often be combined in quadrature to provide an estimate of the overall uncertainty (ISO 1995). Unless stated otherwise, all values given in this book, whether

for individual parameters or for cumulative values, are given as one SD.

If there is a type B uncertainty, such as a systematic offset, then every effort should be made to eliminate the uncertainty since it is known to be the result of an incorrect procedure. In some situations, however, the user knows a type B uncertainty exists but may not have control over the elimination of the uncertainty. This is typical for a TPS where the dose calculation algorithm may have a reproducible deviation from the measured value at certain points within the beam, e.g., at points in or near the penumbra region. Although it is recognized that there is a reproducible difference, the user may not be able to adjust for this difference without causing larger differences elsewhere.

The established practice of radiotherapy shows that reproducibility of dose delivery is critical when considering one facility and one radiation modality. When results between facilities or between modalities are compared, some type B uncertainties may also be important. On the other hand, some type B uncertainties may be common to all participants and can therefore be omitted from routine consideration; e.g., if all the participants follow the same dosimetry protocol, or if the same basic physics data are used in multiple protocols.

The deviation of a measured or calculated result is the difference between its value and an expected value obtained via some other method. The expected value is called the “reference” value. As will be discussed in chapters 8 and 10, reference values are often obtained from commissioning measurements. Tolerance is strictly defined as the range of acceptability beyond which corrective action is required. The choice of a tolerance value, as it is discussed in chapter 8 can therefore be dependent on the uncertainty attributed to the reference value. For example, the tolerance levels for positioning accuracy associated with small field size ion beam treatments, such as used for stereotactic radiosurgery, will be substantially tighter than for large field portals.

In the present book, an **error** is defined as the deviation of a given quantity following an incorrect procedure. Errors can be made even if the result is within tolerance. However, the significance of the error will depend upon the proximity of the result to the tolerance, with results near the tolerance having relatively small significance and results outside of the tolerance range being of more concern, effectively unacceptable.